

Discrete multi-step phase hologram for high frequency acoustic modulation

Meng-Qing Zhou(周梦晴), Zhao-Xi Li(李照希), Yi Li(李怡), Ye-Cheng Wang(王业成), Juan Zhang(张娟), Dong-Dong Chen(谌东东), Yi Quan(全熠), Yin-Tang Yang(杨银堂), and Chun-Long Fei(费春龙)
Citation: Chin. Phys. B, 2024, 33 (**1**): 014303. DOI: 10.1088/1674-1056/acf44c
Journal homepage: http://cpb.iphy.ac.cn; http://iopscience.iop.org/cpb

What follows is a list of articles you may be interested in

Dynamics of magnetic microbubble transport in blood vessels

Jie Chen(陈杰), Chenghui Wang(王成会), and Runyang Mo(莫润阳)
Chin. Phys. B, 2023, 32 (**9**): 094302. DOI: 10.1088/1674-1056/aca14b

Theory of complex-coordinate transformation acoustics for non-Hermitian metamaterials

Hao-Xiang Li(李澔翔), Yang Tan(谭杨), Jing Yang(杨京), and Bin Liang(梁彬)
Chin. Phys. B, 2023, 32 (**9**): 094301. DOI: 10.1088/1674-1056/acc3fc

Bubble nucleation in spherical liquid cavity wrapped by elastic medium

Xian-Mei Zhang(张先梅), Fan Li(李凡), Cheng-Hui Wang(王成会), Jing Hu(胡静), Run-Yang Mo(莫润阳), Zhuang-Zhi Shen(沈壮志), Jian-Zhong Guo(郭建中), and Shu-Yu Lin(林书玉)
Chin. Phys. B, 2023, 32 (**6**): 064303. DOI: 10.1088/1674-1056/acaa30

Characteristic analysis of scattering field in two-layer media by Green's function

Ping Zhang(张萍), Zhi-Ying Liu(刘智颖), Shou-Guo Yan(阎守国), Juan Huang(黄娟), and Bi-Xing Zhang(张碧星)
Chin. Phys. B, 2023, 32 (**6**): 064301. DOI: 10.1088/1674-1056/aca3a0

Deep learning for image reconstruction in thermoacoustic tomography

Qiwen Xu(徐启文), Zhu Zheng(郑铸), and Huabei Jiang(蒋华北)
Chin. Phys. B, 2022, 31 (**2**): 024302. DOI: 10.1088/1674-1056/ac0dab

---

Discrete multi-step phase hologram for high frequency acoustic modulation

Meng-Qing Zhou(周梦晴), Zhao-Xi Li(李照希)[†], Yi Li(李怡), Ye-Cheng Wang(王业成), Juan Zhang(张娟), Dong-Dong Chen(谌东东), Yi Quan(全熠), Yin-Tang Yang(杨银堂), and Chun-Long Fei(费春龙)[‡]

School of Microelectronics, Xidian University, Xi'an 710071, *China*

(Received 5 July 2023; revised manuscript received 11 August 2023; accepted manuscript online 28 August 2023)

Acoustic holograms can recover wavefront stored acoustic field information and produce high-fidelity complex acoustic fields. Benefiting from the huge spatial information that traditional acoustic elements cannot match, acoustic holograms pursue the realization of high-resolution complex acoustic fields and gradually tend to high-frequency ultrasound applications. However, conventional continuous phase holograms are limited by three-dimensional (3D) printing size, and the presence of unavoidable small printing errors makes it difficult to achieve acoustic field reconstruction at high frequency accuracy. Here, we present an optimized discrete multi-step phase hologram. It can ensure the reconstruction quality of image with high robustness, and properly lower the requirement for the 3D printing accuracy. Meanwhile, the concept of reconstruction similarity is proposed to refine a measure of acoustic field quality. In addition, the realized complex acoustic field at 20 MHz promotes the application of acoustic holograms at high frequencies and provides a new way to generate high-fidelity acoustic fields.

Keywords: discrete multi-step phase hologram, econstruction quality, 3D printing accuracy, high-fidelity

PACS: 43.35.+d, 43.60.Sx **DOI:** 10.1088/1674-1056/acf44c

1. Introduction

The strategic modulation of acoustic wavefronts paves the way for the reconstruction of highly diverse acoustic fields and the subsequent retrieval of the essential information that is necessary for wavefront storage. This sophisticated process empowers precision in the manipulation of ultrasound beams to sculpt the acoustic field.[1–4] As a result, it dramatically elevates the quality of ultrasound imaging in the realm of biomedicine.[5–7] Furthermore, this technique is instrumental in facilitating particle manipulation[8–11] in a broad spectrum of ultrasound applications. At present, the acoustic beam is mainly manipulated by phased array ultrasonic transducers,[12–15] self-focusing mechanisms,[16–18] holograms,[19–25] *etc*. In contrast to conventional techniques, acoustic holography is usually fabricated by the rapidly developing three-dimensional (3D) printing technology, which allows mapping the output of the unitary transducer onto a pre-calculated phase map[19] and creating a high-fidelity ultrasound field. In addition, acoustic holography can be well scaled to higher information content than commercial phased-array and self-focusing mechanisms. With its high cost-effective and high freedom degree of reconstruction,[20,26–28] which makes it widely applicable to various transmitting and reflecting elements.

The static phase plates or holograms with a large spatial information content enable acoustic fabrication,[29] cell assembly of design patterns,[30] beam steering,[31] and wavefront distortion compensation in transcranial focused ultrasound.[7] Recently, Ma *et al.*[27,32] have generated rewriteable bubble masks through electrolysis or optically induced electrochemical interactions to achieve dynamic modulation of the holographic wavefront. However, this approach may deviate from the desired acoustic field, owing to the instability of the bubbles which is technically challenging. Holograms pursue high-fidelity implementation of complex acoustic fields at high frequencies, where the rise in frequency greatly increases the complexity of the designed static ultrasound fields, and the high precision print size is often accompanied by robust instability and randomly introduced undesirable errors. At the same time, the metrics for the quality of the reconstructed ultrasound fields is still inadequate and imperfect. At present, only the binary amplitude modulation capability of the incident field has been demonstrated, limiting the efficiency of coupling energy to the desired field to 10%.[33] It is fair to state that the majority of acoustic hologram research is still in the low-frequency phase, where the attainable spatial bandwidth product (SW_H) is restricted by printer size or the reconstructed beam profile range. This leads to a simpler target acoustic field that can be achieved by holograms, such as common single point focusing.[34–36] The demand for higher resolution patterning capabilities at higher frequencies has escalated, making the implementation of continuous phase acoustic holograms challenging in terms of 3D printing accuracy. Yet, the current 3D printing technology[37] is expen-

[†]Corresponding author. E-mail: lizhaoxi@xidian.edu.cn
[‡]Corresponding author. E-mail: clfei@xidian.edu.cn

© 2024 Chinese Physical Society and IOP Publishing Ltd

sive and time-consuming for precisely achieving high printing accuracy, so the mainstream 3D fast printing cannot realize the production of continuous-phase holographic panels with enough fineness.

In this study, we introduce an innovative computational approach for acoustic holography. In the inversion process, we numerically divide the continuous phase information of initial plane into discrete phase information with equal spacing, and demonstrate a discrete multistage step phase holographic plate created with 3D printing technology. Concurrently, we introduce the concept of reconstruction similarity, which refines the metric for characterizing the acoustic field. Under equivalent printing conditions, the reconstruction quality of the optimized multi-step phase (four-step or eight-step) holograms aligns closely with conventional phase holograms. It is applicable to the realization of complex acoustic fields at high frequencies, ensuring robust image reconstruction quality, and reasonably reducing the requirement for 3D printing accuracy. In addition, the realization of 20-MHz composite acoustic field has greatly promoted the development of high-frequency holograms, from scientific research to practical applications.

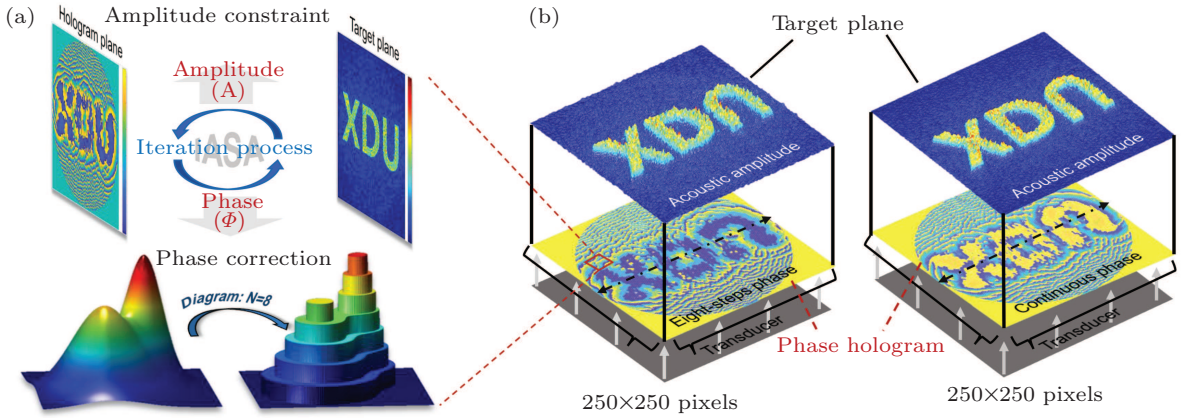


Fig. 1. (a) General flow of iterative angular spectrum approach of reconstructing the acoustic field, along with a correction diagram from continuous phase to eight-step phase, and (b) ultrasonic transducer combined with the corresponding hologram for acoustic field reconstruction.

2. Methods

2.1. Calculation of multi-step phase holograms

Like optical holograms, acoustic holograms accomplish meticulous control of sound waves via sophisticated holographic projections. In order to keep the accurate phase term during propagation, we use iterative angular spectrum approach (IASA) to optimize the calculation of holograms and generate high-fidelity holograms stably[19] (see Fig. 1).

According to IASA, given that the angular spectrum of the holographic plane ($z = 0$) is $P(k_x, k_y, 0)$, the angular spectrum of the z_d plane can be calculated by multiplying it by the propagation function $H(k_x, k_y, z_d)$ as follows:

$$P(k_x, k_y, z_d) = P(k_x, k_y, 0) H(k_x, k_y, z_d), \tag{1}$$

$$H(k_x, k_y, z_d) = \mathrm{e}^{\mathrm{j} z_d \sqrt{k^2 - k_x^2 - k_y^2}}, \tag{2}$$

where $|k| = \omega/c$ is the wavenumber in the liquid medium, ω is the angular frequency, c is the speed of sound in the medium, and $k = (k_x, k_y, k_z)$ is the wave vector. Then the angular spectrum of the target plane, obtained from the forward calculation, is inferred back to the angular spectrum of the 0-plane by the formula

$$P(k_x, k_y, 0) = P(k_x, k_y, z_d) H(k_x, k_y, -z_d). \tag{3}$$

In this work, we take the ideal region "XDU" with amplitude 1 (others are all 0) as the amplitude constraint in the target plane, and modify the phase information of the holographic plane in the iterative process so that its continuous phase is discretized into an equally spaced multi-step phase distribution, as shown below:

$$\phi = \begin{cases} 0, & 0 < \phi \le \dfrac{2\pi}{N}, \\ \vdots & \\ (n-1)\dfrac{2\pi}{N}, & (n-1)\dfrac{2\pi}{N} < \phi \le n\dfrac{2\pi}{N}, \\ \vdots & \\ (N-1)\dfrac{2\pi}{N}, & (N-1)\dfrac{2\pi}{N} < \phi \le 2\pi, \end{cases} \tag{4}$$

where $n \in [1, N]$, N is the total number of equally spaced multi-step phases and n is the n-th order in the multi-step phase.

To compare the ability of different gradient phases to shape the acoustic field, as shown in Eqs. (5)–(8), we set N to 2, 4, and 8, respectively, to obtain the final phase distribution of the holographic plane shown in the upper right inset in Fig. 2(a), respectively.

$$\phi = \begin{cases} 0, & 0 < \phi \le \pi, \\ \pi, & \pi < \phi \le 2\pi, \end{cases} \tag{5}$$

$$\phi = \begin{cases} 0, & 0 < \phi \le \dfrac{\pi}{2}, \\ \dfrac{\pi}{2}, & \dfrac{\pi}{2} < \phi \le \pi, \\ \pi, & \pi < \phi \le \dfrac{3\pi}{2}, \\ \dfrac{3\pi}{2}, & \dfrac{3\pi}{2} < \phi \le 2\pi. \end{cases} \tag{6}$$

By analogy, the equation for the eight-step phase hologram is shown in Eq. (7), while the final equally spaced multi-step phase diagram of any holographic plane can be calculated by expanding Eq. (4).

$$\phi = \begin{cases} 0, & 0 < \phi \le \dfrac{\pi}{4}, \\ \vdots & \\ \dfrac{3\pi}{4}, & \dfrac{3\pi}{4} < \phi \le \pi, \\ \vdots & \\ \dfrac{7\pi}{4}, & \dfrac{7\pi}{4} < \phi \le 2\pi. \end{cases} \tag{7}$$

According to the final phase diagram of the plane, the initial thickness T_0 is used to remove the change amount of the thickness at the pixel position, which causes the phase change $\Delta T(x, y)$, and the final acoustic holographic thickness $T(x,y)$ can be obtained. Since the phase distribution of the original hologram is discretized into multi-step phase information, the acoustic hologram with discrete phase can be calculated from the following equation:

$$\Delta\phi(x,y) = \frac{2\pi(N-1)}{N} = (k_{\mathrm{m}} - k_{\mathrm{h}})\Delta T(x,y), \tag{8}$$

$$T(x,y) = T_0 - \Delta T(x,y), \tag{9}$$

where k_{m} is the wave number in the water and k_{h} is the wave number in the 3D printed acoustic hologram. According to the above steps, the map of final printed acoustic holographic thickness is shown in Fig. 2.

With the number of steps increasing, the discrete phase gradually converges to the continuous phase. Considering a variety of factors, such as printing accuracy and manufacturing difficulty, we select four kinds of acoustic holograms for printing in order to better make a comparative choice according to the needs. In addition to three discrete multi-step phase holograms described above, we make N tend to infinity while obtaining the conventional continuous phase computed acoustic hologram by 3D printing (printing accuracy: 100 μm), as shown in the upper right inset of Fig. 2(a). The detailed information about 3D printed holograms is provided in supplemental material S1. We define the same parameters in advance for these four kinds of acoustic holograms, *i.e.*, design frequency ($f = 3$ MHz), target plane ($z = 30$ mm), and transducer size ($R = 25$ mm).

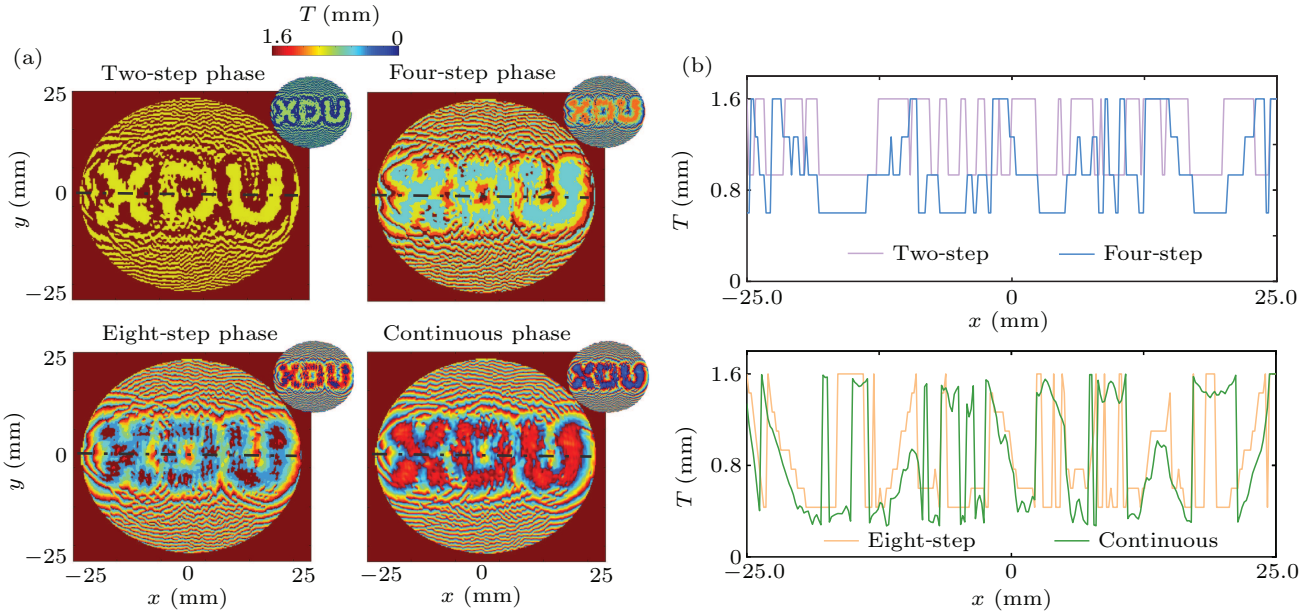


Fig. 2. (a) Thickness distribution and phase distribution (top right inset) of acoustic holograms calculated for discrete multi-step (two-step, four-step, and eight-step) phases and continuous phases, and (b) variations of acoustic holographic thickness $T(x,y)$ with x, corresponding to the black cut-off line (top: two-step and four-step, bottom: eight-step and continuous).

2.2. Measurement of acoustic pressure field

The motion scan acquisition system and the experimental setup are schematically shown in Fig. 3(a). Figure 3(b) shows the multi-step phase hologram, which is positioned on the surface of the transducer with a central frequency of 3 MHz. Detailed specifications of the transducer can be found in supplemental material S1. The sound pressure fields in the x–y plane of these four multi-step holograms are gauged by using a custom-built, multi-functional ultrasonic testing system. This system is constructed based on LabVIEW software in conjunction with a needle hydrophone (NA1000, PA, UK).

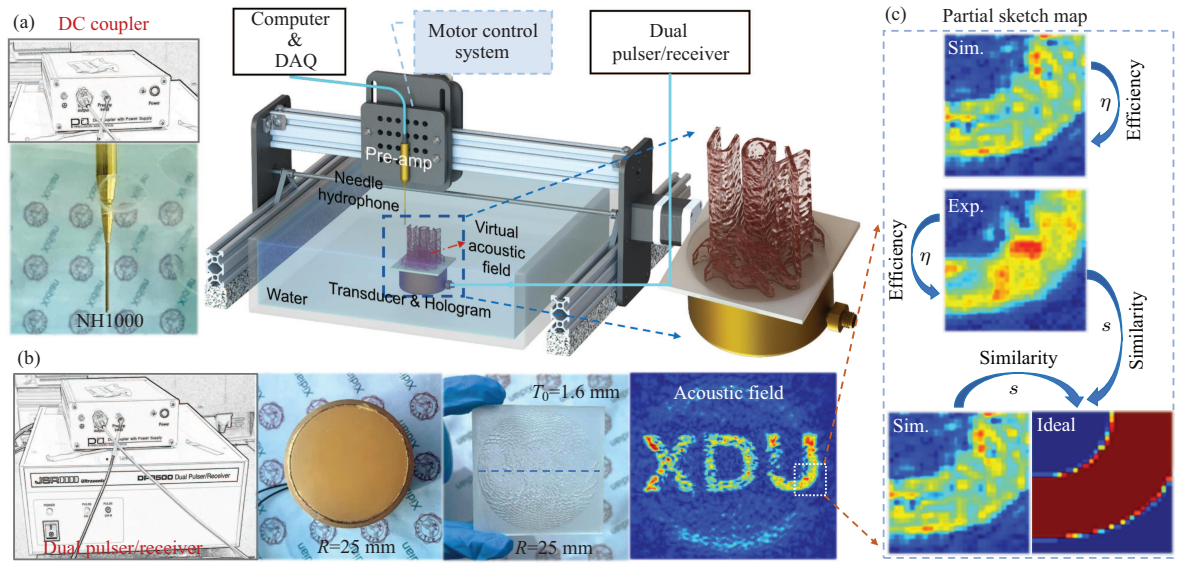


Fig. 3. (a) Schematic diagram of motor control system and equipment to be tested. (b) Experimental setup for testing actual object. (c) Sketch map of partial calculation of image reconstruction efficiency and reconstruction similarity.

During the test, the ultrasonic dual pulser/receiver is taken in conjunction with a needle hydrophone (NA1000, PA, UK). The ultrasonic dual pulser/receiver (DPR500, JSR Ultrasonics, USA) generates a pulse excitation signal. This signal is subsequently applied to the ultrasonic transducer to produce the ultrasonic pressure field. Finally, the sound pressure field within a rectangular area of 52 mm×52 mm (x–y plane) is measured by using a hydrophone with a precision of 200 μm.

3. Results and discussion

3.1. Image uniformity evaluation

In this work, the acoustic field simulation is performed on condition that the acoustic field is augmented by a factor of 4 to minimize the adverse effects of boundary effects. Based on the defined transducer plane diameter of 50 mm, each grid is a square with a size of 200 μm (less than half a wavelength), so on the basis of magnification, the effective area is finally selected in the imaging plane, i.e., it contains a structure of 250×250 pixels, as shown in Fig. 4. As mentioned above, its phase map is encoded and printed in the hologram, and reconstructed in water with 3-MHz ultrasound. The number of individually accessible pixels in the hologram that creates the acoustic field directly affects the amount of information contained in it. To further describe the image distribution, the concept of image uniformity is proposed.

The normalized sound pressure amplitude distributions of four phase acoustic holograms are obtained by calculation and experiment as shown in Fig. 4. The comparison of simulation calculations with experimental results shows that its distribution has a certain regularity. The absolute sound pressure distribution produced by the two-step phase hologram is relatively dispersed as shown in Figs. 4(a) and 4(b), which suggests that the acoustic field is lacking in fine detail and relatively rough. The four-step phase and the eight-step phase holograms produce a finer distribution of sound pressure, mainly concentrated on the letters "XDU" and with higher values. The accuracy of the 3D printed acoustic hologram gradually declines and approaches the complexity of continuous phase printing as the number of phase steps increases (detailed explanation in supplemental material S2), but it is still considerably better than that generated by two-step phase.

Figures 4(c)–4(g) show the distribution curves of the relationship between the number of pixel points and the generated sound pressure value of the four-step phase simulation and experiments. Here, the sound pressure values are normalized and the range of sound pressure values from 0 to 1 is divided into ten equal intervals. In Figs. 4(c) and 4(d), the pixels on the letter "XDU" are mainly distributed between 0.4 and 0.7. The two-step phase has the most pixel distribution when the sound pressure values are at 0.4 (experimental value) and 0.5 (simulation value). Comparing with the two-step phase, the number of pixels in the four-step phase is gradually distributed evenly, and the hologram of the eight-step phase and the hologram of continuous phase are both mainly concentrated at the sound pressure value 0.6 and gradually approaches 1. Figures 4(f) and 4(g) mainly display the number distributions of pixels outside the letter "XDU" in four cases. Figure 4(g) shows the significantly interfering data in the two-step image, with the undesired fraction concentrated below the 0.2 sound pressure value when the phase is set to four-step phase and eight-step phase. Thus, uniformity and high fidelity similar to that of conventional (ideal) continuous phase can still be achieved. The errors between the experimental results and simulation values for these four holograms in Fig. 4(e) are due to the presence of shear waves in the experimental lens as well as acoustic wave attenuation, which are neglected in the present simulation.

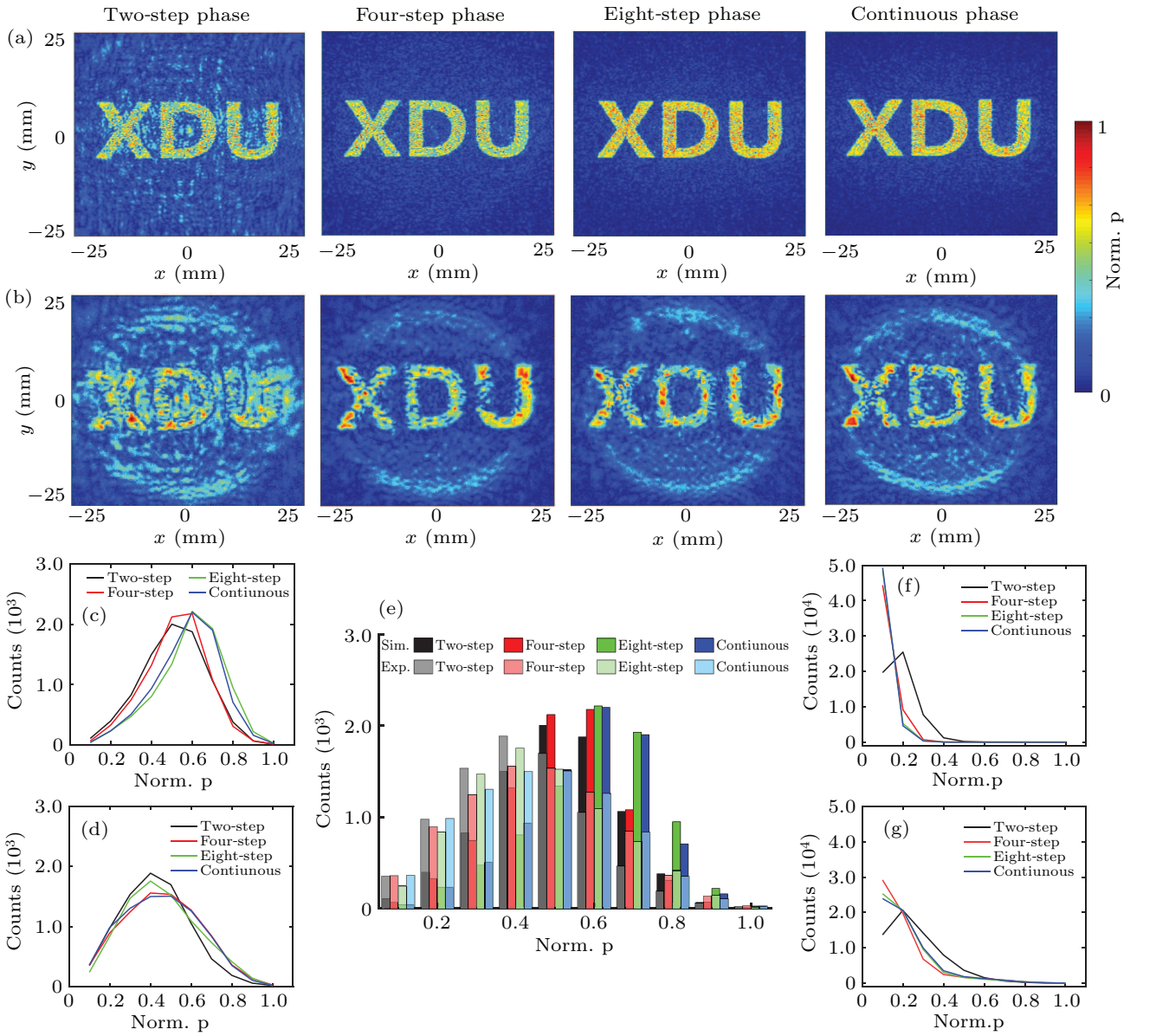


Fig. 4. [(a), (b)] Normalized sound pressure (Norm. p) amplitude distributions in x–y plane ($z = 30$ mm) calculated by IASA and scanned by hydrophone, respectively, showing two-step phase, four-step phase, eight-step phase, and continuous phase from left to right. (c) Simulated and (d) measured pixel distribution on the "XDU" letter area of the target image, (f) simulated and (g) measured pixel distribution in the area other than the "XDU" area corresponding to the four phases. (e) Comparison between simulated and measured numbers of pixels in "XDU" region for four holograms.

As a result, the quantitative evaluations of visual effects and image homogeneity by the naked eye show that our multi-order phases are able to reduce manufacturing difficulties and that the fourth and higher order phases can simultaneously ensure a homogeneous distribution of images with major sound pressure values above 0.5.

3.2. Image reconstruction quality evaluation

Relating the sound power of the target region within the acoustic field to the sound power of the entire image acoustic field[19] enables a better assessment of the effectiveness of the reconstructed image, thus using the overall reconstruction efficiency η as a representation of the quality of the acoustic field reconstruction. According to the relationship among sound pressure, sound intensity and sound power, the formula for sound power can be finally expressed in terms of sound pressure, as given by

$$P_z = \Delta x \Delta y \sum_{(i,j)\in I} I_{z,(i,j)} = \Delta x \Delta y \sum_{(i,j)\in I} \frac{p^2_{z,(i,j)}}{2\rho c_{\mathrm{m}}}, \tag{10}$$

where (i, j) is the location of each pixel point; Δx and Δy are the sampling distances (pixel size) along the x coordinate and y coordinate, respectively, in the observation plane.

The reconstruction efficiency can be expressed as follows:

$$\eta = \frac{P_{z,T}}{P_z} = \frac{\sum\limits_{(i,j)\in T} p^2_{z,(i,j)}}{\sum\limits_{(i,j)\in I} p^2_{z,(i,j)}}, \tag{11}$$

where the target region T is the actual pixel set corresponding

to the position where the ideal image is greater than 0 amplitude after 50 iterative calculations. The whole image I is a set of pixels with all values after calculation.

However, in general, the quality of acoustic field reconstruction cannot be described solely in terms of sound energy utilization;, and it is also related to reconstruction accuracy. When calculating and analyzing the efficiency, the most important premise is to calculate the sound pressure within the area corresponding to the ideal "XDU". Therefore, it is necessary to evaluate the reconstruction similarity of the "XDU" letter between the acoustic field of the actual target area T and the acoustic field of the ideal target area D.

The above correction of Eq. (11) leads to the formula for reconstructing similarity

$$s = \frac{\sum_{(i,j)\in T} p_{z,(i,j)}^2}{\sum_{(i,j)\in D} p_{z,(i,j)}^2}, \tag{12}$$

where D is the target acoustic field area of non-zero amplitude on the letter "XDU" in the ideal case.

The schematic diagram of the local calculation of the reconstructed image quality is shown in Fig. 3(c). Before comparing its reconstruction efficiency, it is necessary to analyze the reconstruction similarity first, thereby fully characterizing the quality of the whole acoustic field image reconstruction. Table 1 gives the reconstruction similarity for two-step phase, four-step phase, eight-step phase, and continuous phase, as indicated by simulation and experiment.

Table 1. Reconstruction similarity between multi-step phase and continuous phase.

	Two-step	Four-step	Eight-step	Continuous
Simulation	26.29	27.04	35.37	33.29
Experiment	18.54	22.60	22.03	21.98

Table 2 then shows the reconstruction efficiencies in these four cases. For these four types, it is obvious that the reconstruction similarity between the two-step phase and the four-step phase is relatively close to each other, but their reconstruction efficiencies are significantly different, which indicates that the two-step phase produces more interference data outside the "XDU" letters and there is obvious scattering of acoustic field. When the phase information is set to the eight-step phase information, the reconstruction similarity and the reconstruction efficiency are almost better than the those of continuous phase.

This is because the eight-step phase hologram's complexity makes it difficult to distinguish between the actual step and an erroneous one that is not simply minor in comparison with the step in the best scenario. The C-mode scans of the four holograms are performed by a 100-MHz high-frequency ultrasound transducer, and the mean absolute percentage errors (MAPEs) of 3D printing are verified to be 9.87%, 10.88%, 45.51%, and 50.39%, respectively. Details of the four hologram thickness variations are given in supplemental material S2. Therefore, in the case where the 3D printing accuracy cannot meet the higher requirements of continuous phase acoustic holograms, the effect of four-step phase and eight-step phase acoustic holograms are more likely to meet the target requirements.

Table 2. Reconstruction efficiency between multi-step phase and continuous phase.

	Two-step	Four-step	Eight-step	Continuous
Simulation	60.62	85.45	91.94	92.47
Experiment	34.43	63.62	58.42	54.69

Increasing the frequency from 3 MHz to 20 MHz will be more stringent on the accuracy of the printer. The quick creation of high frequency holograms cannot be supported by the 100-μm printing precision being used at present time. In order to simply compare the feasibility of using step phases for their high frequencies, as shown in Fig. 5(a), only four-step and continuous-phase high-frequency holograms are generated with only 10-μm printing accuracy. Figures 5(b) and 5(c) show the simulated and measured normalized sound pressure amplitude diagram of four-step phase and continuous phase at a frequency of 20 MHz. In the same printing conditions, the reconstruction similarity and reconstruction efficiency of the four-step hologram, calculated in the experiment (simulation), are 18.03% (simulation: 30.77%) and 41.81% (simulation: 86.27%), and the reconstruction efficiency of continuous holograms are 17.94% (simulation: 33.07%) and 40.71% (simulation: 92.80%), respectively. In order to better characterize the contouring errors occurring in the 3D printing process, C-mode scanning of hologram is performed by a 100-MHz high-frequency ultrasonic transducer, in which the error of the four-step holograms is only 11.77%, whereas the printing error of continuous holograms can even reach more than 20%. The thickness variation of the 20-MHz phase hologram scanned by C-mode is given in supplemental material S2. Like the results in the low-frequency condition, the four-step hologram possesses a better image reconstruction quality. With the development of high frequency in demand, the implementation of multi-step holograms to a certain extent can not only reduce the influence caused by the printing error as much as possible, but also maintains the reconstruction quality of complex acoustic fields. It can be shown that the optimized multi-step phase hologram can be better applied to high frequency scenarios when the desired frequency is gradually increased.

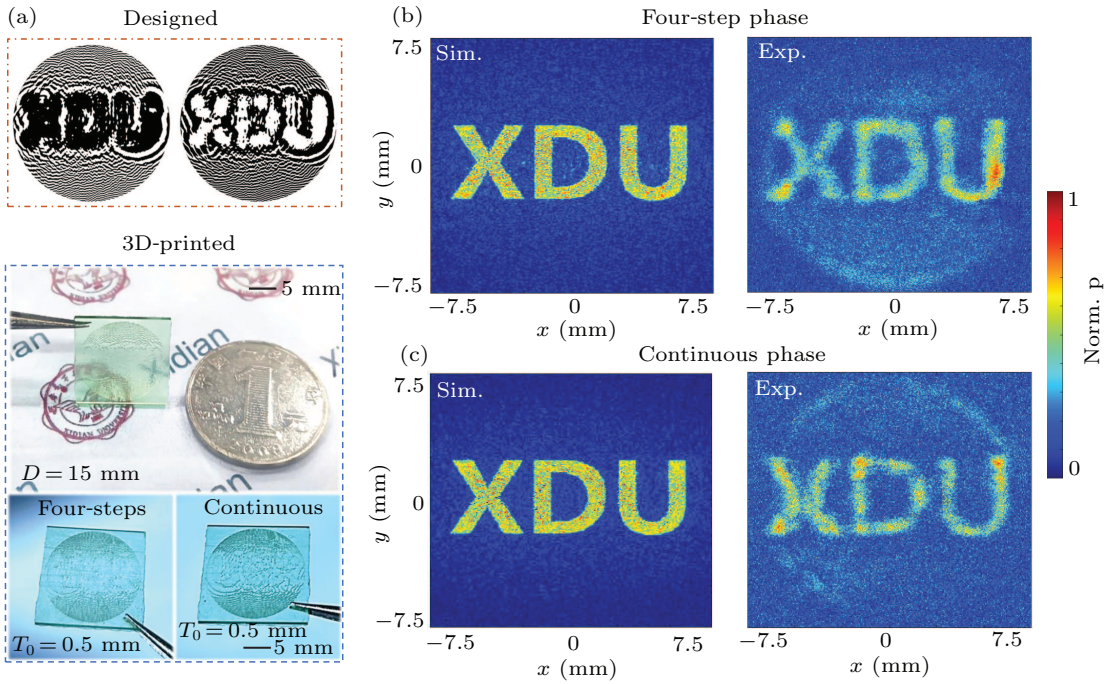


Fig. 5. (a) Designed and 3D printed hologram with generated letters "XDU". (b) and (c) Normalized sound pressure amplitude distribution (left side: simulation, right side: experiment) in x–y plane ($z = 15$ mm) generated by IASA calculations and hydrophone scanning with four-step phase (top row) and continuous phase (bottom row).

Generally, the ability to store encoded acoustic field information in holograms is constrained by a finite flat aperture in the transmission of sound waves to the target image distance, thereby making it impossible to achieve 100% perfect image reconstruction quality. By comparing with the ideal value, the mean square error can be used to calculate the error of reconstruction similarity. The mean square errors of two-step, four-step, eight-step, and continuous phase simulations are 3.36%, 3.13%, 2.31%, and 2.49%, respectively. In addition, the experimental errors are 4.81%, 4.25%, 4.26%, and 4.39%, owing to the coupling and attenuation of the acoustic waves in the medium, respectively.

4. Conclusions

In this work, we presented a computational technique for discrete multi-step phase acoustic holograms, which is based on the optimization of the iterative angular spectrum approach. In the present method the conventional continuous phase is discretized into uniformly spaced multi-step phases, thereby generating corresponding acoustic holograms. We also introduced the concept of reconstruction similarity, an improved measure that can characterize the acoustic field image quality more evenly.

Under equivalent printing conditions, the unavoidable errors associated with 3D printing lead the image reconstructions for eight-step and continuous phase-based holograms to lower their quality. Furthermore, the hydrophone scanning results for the ultrasound field differ from the simulation results. Our findings indicate that four-step or eight-step holograms can ensure higher reconstruction quality and greater robustness when the accuracy of 3D printing cannot satisfy the more stringent requirements of continuous phase holograms. Additionally, the discrete multi-step phase technique can be adopted in the implementation of complex acoustic fields at 20 MHz, which can greatly promote the development of high-frequency acoustic fields, from scientific exploration to practical applications.

Data availability statement

The data that support the findings of the present study are openly available in Science Data Bank at https://doi.org/10.57760/sciencedb.j00113.00153.

Acknowledgements

Project supported by the China Postdoctoral Science Foundation (Grant No. 2023M732745), the National Natural Science Foundations of China (Grant Nos. 61974110 and 62104177), the Fundamental Research Funds for the Central Universities, China (Grant Nos. QTZX23022 and JBF211103), and the Cooperation Program of XDU–Chongqing IC Innovation Research Institute (Grant No. CQ IRI-2022CXY-Z07).

References

[1] Kruizinga P, Pim van der Meulen, Fedjajevs A, Mastik F, Springeling, Nico de Jong G, Bosch J G and Leus G 2017 *Sci. Adv.* **3** e1701423
[2] Collins D J, Ma Z C, Han J Y and Ai Y 2017 *Lab Chip* **17** 91
[3] Baudoin M, Thomas J L, Sahely R A, Gerbedoen J C, Gong Z, Sivery A, Matar O B, Smagin N, Favreau P and Vlandas A 2020 *Nat. Commun.* **11** 4244

[4] Memoli G, Caleap M, Asakawa M, Sahoo D R, Drinkwater B W and Subramanian S 2017 *Nat. Commun.* **8** 14608
[5] Maimbourg G, Houdouin A, Deffieux T, Tanter M and Aubry J F 2018 *Phys. Med. Biol.* **63** 025026
[6] Hirayama R, Martinez Plasencia D, Masuda N and Subramanian S 2019 *Nature* **575** 320
[7] Jiménez-Gambín S, Jiménez N, Benlloch J M and Camarena F 2019 *Phys. Rev. Appl.* **12** 014016
[8] Marzo A, Caleap M and Drinkwater B W 2018 *Phys. Rev. Lett.* **120** 044301
[9] Li J F, Crivoi A, Peng X Y, Shen L, Pu Y J, Fan Z and Cummer S A 2021 *Commun. Phys.* **4** 113
[10] Yang Y, Ma T, Li S N, Zhang Q, Huang J Q, Liu Y F, Zhuang J W, Li Y C, Du X M, Niu L L, Xiao Y, Wang C Z, Cai F Y and Zheng H R 2021 *Research* **2021** 9781394
[11] Lam K H, Hsu H S, Li Y, Lee C Y, Lin A, Zhou Q F and Shung K K 2013 *Biotechnol. Bioeng.* **110** 881
[12] Marzo A, Seah S A, Drinkwater B W, Sahoo D R, Long B and Subramanian S 2015 *Nat. Commun.* **6** 8661
[13] Marzo A and Drinkwater B W 2019 *Proc. Natl. Acad. Sci. USA* **116** 84
[14] Ochiai Y, Hoshi T and Rekimoto J 2014 *PloS One* **9** e102525
[15] Hu H J, Zhu X, Wang C H, Li X S, Lee S, Huang Z L, Chen R M, Chen Z Y, Wang C F, Gu Y, Chen Y M, Lei Y S, Zhang T J, Kim N, Guo Y X, Teng Y, Zhou W B, Li Y, Nomoto A, Sternini S, Zhou Q F, Pharr M, Lanza Di Scalea F and Xu S 2018 *Sci. Adv.* **4** eaar3979
[16] Zhu B P, Fei C L, Wang C, Zhu Y H, Yang X F, Zheng H and Shung K K 2017 *ACS Sens.* **2** 172
[17] Gao H, Gu Z M, Liang B, *et al*. 2016 *Appl. Phys. Lett.* **108** 073501
[18] Fan Q B, Wang D P, Huo P C, Zhang Z J, Liang Y Z and Xu T 2017 *Opt. Express* **25** 9285
[19] Melde K, Mark A G, Qiu T and Fischer P 2016 *Nature* **537** 518
[20] Brown M D, Cox B T and Treeby B E 2023 *Phys. Rev. Appl.* **19** 044032
[21] Gu Y Y, Chen C Y, Rufo J, Shen C, Wang Z Y, Huang P H, Fu H, Zhang P R, Cummer S A, Tian Z H and Huang T J 2020 *ACS Nano* **14** 14635
[22] Shakya G, Yang T, Gao Y, Fajrial A K, Li B, Ruzzene M and Ding X 2022 *Nat. Commun.* **13** 987
[23] Tamulevičius T, Juodėnas M, Klinavičius T, Paulauskas A, Jankauskas K, Žutautas A and Tamulevičius S 2018 *Sci. Rep.* **8** 14245
[24] Zheng G X, Mïhlenbernd H, Kenney M, Li G X, Zentgraf T and Zhang S 2015 *Nat. Nanotechnol.* **10** 308
[25] Li J X, Kamin S, Zheng G X, Neubrech F, Zhang S and Liu N 2018 *Sci. Adv.* **4** eaar6768
[26] Fushimi T, Yamamoto K and Ochiai Y 2021 *Sci. Rep.* **11** 12678
[27] Ma Z C, Melde K, Athanassiadis A G, Schau M, Richter H, Qiu T and Fischer P 2020 *Nat. Commun.* **11** 4537
[28] Cox L, Melde K, Croxford A, Fischer P and Drinkwater B W 2019 *Phys. Rev. Appl.* **12** 064055
[29] Melde K, Choi E, Wu Z G, Palagi S, Qiu T and Fischer P 2018 *Adv. Mater.* **30** 1704507
[30] Ma Z C, Holle A W, Melde K, Qiu T, Poeppel K, Kadiri V M and Fischer P 2020 *Adv. Mater.* **32** 1904181
[31] Li Z X, Fei C L, Yang S H, Hou C X, Zhao J X, Li Y and Yang Y T 2022 *Adv. Funct. Mater.* **32** 2209173
[32] Ma Z C, Joh H, Fan D E and Fischer P 2022 *Adv. Sci.* **9** 2104401
[33] Moreno V, Román J F and Salgueiro J R 1997 *Am. J. Phys.* **65** 556
[34] Jin Y B, Kumar R, Poncelet O, Mondain-Monval O and Brunet T 2019 *Nat. Commun.* **10** 143
[35] Vovchuk D, Khobzei M, Filonov D and Ginzburg P 2022 *Sci. Rep.* **12** 2479
[36] Vodo P, Parimi P V, Lu W T and Sridhar S 2005 *Appl. Phys. Lett.* **86** 201108
[37] Habibi M, Foroughi S, Karamzadeh V and Packirisamy M 2022 *Nat. Commun.* **13** 1800